J. Phys. Chem. A **2002,** *106,* 4125−4136 **4125**

Quasiclassical Trajectory and Transition State Theory Studies of the N(^{4}S) + H_2 ↔ NH($X^3\Sigma^-$) + H Reaction

Ronald Z. Pascual

University Laboratory School, University of Southern Mindanao, Kabacan, Cotabato, Philippines 9407

George C. Schatz*

Department of Chemistry, Northwestern University, Evanston, Illinois 60208-3113

György Lendvay

Institute of Chemistry, Chemical Research Center, Hungarian Academy of Sciences,
P.O. Box 17, H-1525 Budapest, Hungary

Diego Troya

Departamento de Química, Universidad de La Rioja, C/Madre de Dios 51, 26006 Logroño, Spain

Received: August 27, 2001; In Final Form: January 29, 2002

Detailed forward and reverse quasiclassical trajectory and variational transition state theory studies of the title reaction are presented. The potential energy surface (PES) has been calculated at the MCQDPT2//FORS-MCSCF(7,6)/6-311++G** level of theory using GAMESS. Selection of points and analytical interpolation of the surface was done using the GROW program of Collins, Thompson, Jordan, and Bettens. Broad ranges of translational energies, and ground and excited rovibrational energy levels (v,j) are chosen as initial conditions of the reactant molecules. All three reactions considered in this study (e.g., N + H_2 and NH + H abstraction and exchange) show angular distributions that are backward peaked. Both the forward abstraction and the exchange reactions show product vibrational distributions that are dominated by the ground state, whereas the reverse reaction prefers $v' = 1$ for trajectories initiated at low E_T. The rate constants for the forward and reverse reactions were found to be in good accord with available experimental and theoretical data and can be expressed in the Arrhenius form as $k(\mathrm{T}) = 6.85 \times 10^{-10} \exp(-25.9(\mathrm{kcal/mol})/RT)$ and $k(T) = 1.85 \times 10^{-14} T^{1.07} \exp(-2.2(\mathrm{kcal/mol})/RT)$ cm^3 molecule^{-1} s^{-1}, respectively. For ICVT results, these rate constants can be similarly expressed as $k(T) = 5.52 \times 10^{-10} \exp(-32.4(\mathrm{kcal/mol})/RT)$ and $k(T) = 1.56 \times 10^{-16} T^{1.64} \exp(-0.7(\mathrm{kcal/mol})/RT)$ cm^3 molecule^{-1} s^{-1}, respectively. The reasonable agreement with the available data substantiates the sufficiency of the computational methods employed in this study.

I. Introduction

Nitrogen atom reactions, particularly with hydrogen, have been a subject of interest among experimental and theoretical chemists for the past three decades. This is understandable since nitrogen-containing compounds play interesting and important roles in atmospheric chemistry, combustion of nitrogen-containing fuels, and explosion processes. The title forward reaction (R1), for instance, is a very important reaction in the thermal decomposition of cyclotrimethylenetrinitramine ($C_3H_6N_6O_6$) and cyclotetramethylenetetranitramine ($C_4H_8N_8O_8$), which are important ingredients in solid propellants used for rockets and guns.[1] Likewise, the reverse title reaction (R−1) is among the series of radical reactions involved in the pyrolysis of ammonia (NH_3) and is thought to play a crucial role in the decay of the imidogen (NH).[2,3]

$$\mathrm{N(^4S)} + \mathrm{H_2} \xrightarrow{k_1} \mathrm{NH(X^3\Sigma^-)} + \mathrm{H} \tag{R1}$$

$$\mathrm{NH(X^3\Sigma^-)} + \mathrm{H} \xrightarrow{k_{-1}} \mathrm{N(^4S)} + \mathrm{H_2} \tag{R−1}$$

$$\mathrm{H} + \mathrm{NH(X^3\Sigma^-)} \rightarrow \mathrm{HN(X^3\Sigma^-)} + \mathrm{H} \tag{R2}$$

Most experimental studies of both forward and reverse reactions have been geared toward the determination of the reaction rate constants. Koshi et al.[4] investigated the forward reaction using direct detection of N atoms by the atomic resonance absorption technique in a shock tube apparatus over the temperature range 1640−2400 K. The rate coefficient for this reaction was found to be $k_1 = (4.6 \pm 0.3) \times 10^{-10} \exp(-33 \pm 7\ (\mathrm{kcal/mol})/RT)$ cm^3 molecule^{-1} s^{-1}. Davidson and Hanson,[5] using a similar experimental method over the temperature range 1950−2850 K determined a smaller preexponential factor (2.7×10^{-10}) and a lower activation energy (25.1 kcal/mol). For the reverse reaction, Morley[6] measured a rate constant value of $k_{-1} = 1.7 \times 10^{-11}$ cm^3 molecule^{-1} s^{-1} for the temperature range 1790−2200 K. Baulch et al.[7] further recommended this value for the temperature range of 1500−2500 K, while Hanson and Salimian[8] suggested $k_{-1} = 5.0 \times 10^{-11}$ cm^3 molecule^{-1} s^{-1} for the temperature range 1790−2200. Likewise, Davidson and Hanson,[5] using the thermodynamic data in the Sandia Database and their k_1 value, gave the equivalent reverse rate coefficient as $k_{-1} = 5.3 \times 10^{-11} \exp(-0.3(\mathrm{kcal/mol})/\mathrm{RT})$ cm^3 molecule^{-1} s^{-1}.

The reaction is also a model system having few electrons and is amenable to high-quality ab initio calculations; hence it has been the subject of several theoretical studies.[9−11] Most ab initio studies carried out for both forward and reverse reactions were conducted mainly to determine stationary point properties,

10.1021/jp0133079 CCC: $22.00

and the rate constants. Koshi et al.[4] optimized the geometries of the stationary points at the HF/4-31G and calculated energies at MP4/6-31G(d,p) levels of theory. They calculated forward and reverse barrier heights for the quartet state reaction which are 35.3 and 4.4 kcal/mol, respectively. These values conform to their experimental results, but are too large compared to Davidson and Hanson's.[5] The two most recent articles also presented direct ab initio variational transition state theory studies to calculate the rate constant. Zhang and Truong[9] were able to calculate the forward and reverse reaction rate constants in the temperature range 400−2500 K by microcanonical variational theory (μVT) using the QCISD(TQ)/cc-pVTZ level of theory. They derived the expressions $k_1 = 3.87 \times 10^{-10}$ exp(−30.8(kcal/mol)/RT) cm^3 molecule^{-1} s^{-1}, and $k_{-1} = 9.26 \times 10^{-16}T^{1.44}$ exp(−0.8(kcal/mol)/RT) cm^3 molecule^{-1} s^{-1}, respectively. These values are in close agreement with those determined by Koshi et al. An earlier canonical variational theory (CVT) calculation using UMP2, UQCISD(T), and MP-SAC4 with the 6-311G** basis set was also conducted by Xu, Fang and Fu[10] to calculate the rate constant of the reverse reaction. They also found good agreement with the experiment of Davidson and Hanson in the temperature range 2000−3000 K. Fu et al.[10] had also compared various lower and higher ab initio levels of theory in calculating the total energies of equilibrium structures for the reverse reaction. They found that the energy of the reaction strongly depends on electronic correlation and on the basis set used. For instance, it was obvious in their study that energies calculated at the UHF level are overestimated; however, the addition of polarization functions reduces the deviation between theory and experiment in the heat of reaction from 18.2 to 9.1 kcal/mol. They added that after the addition of electronic correlation to UHF/6-311G** energies, the reaction barrier height for the reverse reaction drops from 8.6 to 5.3 and 3.1 kcal/mol at the UMP2 and UMP4 level, respectively. Single-point energy calculations at the UQCISD(T) and MP-SAC4 levels give the lowest value for the reaction barrier in their study, which is closest to the experimental value. It is interesting to note that none of these ab initio studies considered multireference (MCSCF or CASSCF) calculations, which are heavily used in other reactions[11,12] and are usually more accurate in characterizing reactions that involve bond breaking/forming and electron transfer. Fu et al., however, carried out a CASSCF-(5,6)/6-311G** to illustrate the feasibility of a UHF single-configuration reference state. Their result showed that the coefficient of the ground-state configuration is 0.982 and those of other configurations are all about 0.1 or less. Hence, they argued that a single ground-state determinant could afford a sufficiently accurate description of this reaction. We will show later in this study that a combination of a CASSCF type calculation using a moderately large basis set and perturbative treatment of dynamical correlation can yield excellent energy and geometric values in comparison with various high-level single-configuration reference state ab initio calculations, and the experimental value.

Despite progress in modern cross-molecular beam techniques,[13] there have been no experimental studies of the ground state of (R1) to determine differential cross sections, and rovibrational and angular distributions of the products. This is due to the difficulty in the preparation of N atoms and NH radicals, although such studies may be possible in the future. The ground-state N(^{4}S) atom is not very reactive, and this is partly the reason there has been significant interest recently in characterizing the reaction dynamics of the lowest excited-state N(^{2}D), a more reactive N atom species.[11] Among the wealth of experimental and theoretical studies conducted for the N(^{2}D) + H_2 reaction have been quantum-mechanical studies,[14] crossed-molecular beam experiments, and quasiclassical trajectory (QCT) studies.[15] These studies were able to shed important insight into its various dynamical properties, including information about the important role of excited potential surfaces that correlate to N(^{2}D) on the thermal rate constant.

In the present study, we use quasiclassical trajectory and variational transition state theory (VTST) calculations to study the dynamics of reactions R1, R−1, and also the exchange reaction (R2) using an accurate potential surface derived from high-quality ab initio calculations. The primary goals of this work are to determine forward and reverse rate constants and to characterize cross sections and product state distribution information that will be useful for interpreting future state-resolved dynamics experiments. In addition, we use this study to test a recently developed Shepard interpolation approach to the representation of ab initio data using analytical functions.

One of the challenges in QCT studies is the development of an accurate PES that fully represents the equilibrium structures, reaction paths (including isomerization processes), and other dynamically important regions of the PES of the reactions. Usually, this task is done by fitting a large number of high-level ab initio points to analytical functions. This procedure is tedious and generally entails a separate but related calibration process using QCT calculations. Recently, a program called GROW was devised by Collins et al.[16] that can largely automate the development of analytical potential surfaces for a wide variety of chemical reactions. In GROW, the PES is constructed using Shepard interpolation of ab initio data that includes the energy, energy gradient, and second derivatives at a large number of molecular configurations. In the present study, we use the GROW program to develop the NHH PES, and in this process we will study the properties of the interpolated surface so as to assess the usefulness of GROW for determining surfaces for use in state-resolved dynamics studies. To do this study, the GROW program was modified to make it work seamlessly with the GAMESS[17] ab initio program, as the original code was optimized for the GAUSIAN 94/98 ab initio program suite. A standard QCT code developed by Schatz et al.[11] was also integrated with GROW for initialization and analysis of the trajectories.

II. Computational Methods

Two groups have already studied (R1)[10,11] at several ab initio levels, but only for determining stationary point properties. In the trajectory calculations, we need the entire surface that is energetically accessible, so some compromises in the ab initio method are needed in order to calculate the surface at the highest possible level that still allows determination of the energy, and its first and second derivatives at a large number of geometries. The ab initio calculations reported in ref 9 can be considered very accurate, as they involve a high level of correlation with a reasonably large basis set (QCISD(TQ)/cc-pVTZ); however a potential fit at such a high level is not feasible. The work in ref 10 was done at relatively low levels of theory, which provide saddle point geometries and barrier heights that are unacceptably far from the high-level results of ref 9. The highest level in ref 10 is the MP4-SAC method, which, however, is not easy to use in automatic calculations and is still not accurate enough. To find a proper level of theory, we ran a series of calculations at various levels. We concluded that CAS-SCF (or FORS-MCSCF) calculations followed by a perturbative treatment of electron correlation leads to results remarkably similar to those

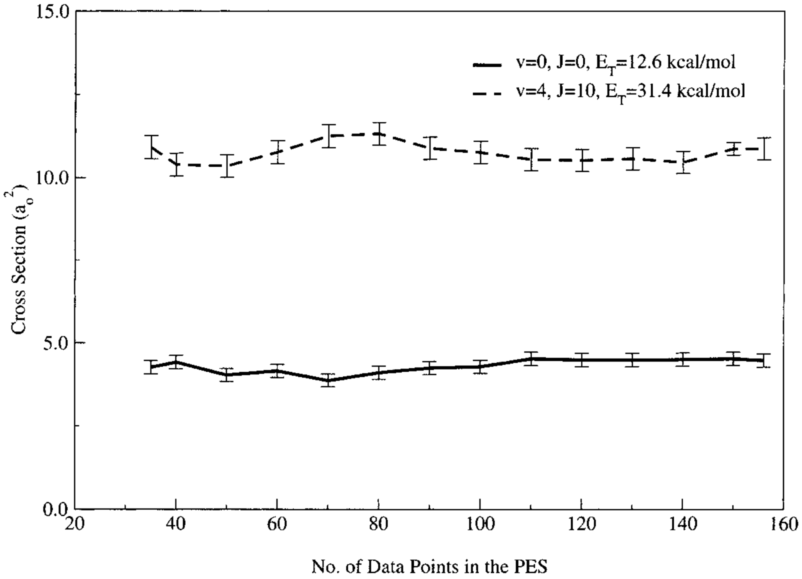

Figure 1. Reactive cross section for NH + H trajectories initiated with $v = 0$, $J = 0$, $E_T = 12.6$ kcal/mol (solid line) and $v = 4$, $J = 10$, $E_T = 31.4$ kcal/mol (dashed line), as the number of data points defining the NHH PES is increased. 2σ error bars are displayed on all trajectory results.

reported in ref 9. The electronic structure calculation here involves multiconfiguration quasidegenerate perturbation theory terminated at second order (MCQDPT2) employing a 6-311++G** basis set. In this calculation, the orbitals were initially optimized using 7 active electrons, 6 active orbitals, and a multiconfiguration, self-consistent wave function of the full optimized reaction space type (FORS-MCSCF), otherwise known as CAS-SCF. The active orbitals included were the H−H σ bonding and antibonding molecular orbitals (MO's), and the N atom's 2s and 2p atomic orbitals, while the nitrogen 1s orbital was kept doubly occupied. We found that a 7 electron, 7 orbital calculation does not yield significant improvement. For convenience, we shall call hereafter the overall ab initio model as MRMP2(7,6)/6-311++G**.

A. Electronic Structure Calculations and Construction of the NHH Potential. Since the original GROW program was optimized to work with the GAUSSIAN 94/98 program suite,[18] significant effort was spent to make changes in the code to make it work under GAMESS.[17] In addition, the initialization routine of GROW, which sets up initial coordinates and momenta for simulation, was not used, as we wanted to use a standard QCT initialization procedure (see below) instead. When the changes were completed, the usual procedures for growing the PES, as outlined by Collins et al.,[16] were followed with some modifications that we now describe.

In the implementation of GROW, 20 molecular configurations from the intrinsic reaction coordinate (IRC) path connecting N + H_2 and NH + H, along with 16 more configurations representing the IRC for the exchange reaction (R2) were used to define an initial surface using Shepard interpolation. Note that each data point includes energy, gradient, and Hessian from the ab initio calculations. Other molecular configurations for inclusion in the data set were then automatically selected by GROW, with two data points chosen for each additional cycle based on trajectory calculations for the NH + H reaction that are described below. For each cycle, one data point was chosen on the basis of the root-mean-square variance of the interpolated energies at regularly sampled points from the trajectories. The other point was based on the weighting function *h* of the trajectory points that is used in the Shepard interpolation.[16] Since we were interested in modeling NH + H collisions with NH in rovibrational states up to NH($v = 4$, $J = 10$), we used this quantum state, a fairly large translational energy, $E_T = 31.4$ kcal/mol, and a small maximum impact parameter, $b_{max} = 1.0$ a_0, as initial conditions for the trajectory calculations in selecting points 37−100 in the growing procedure. An additional 56 points were then added to further refine the surface on the basis of trajectories initiated with $E_T = 12.6$ kcal/mol, NH($v = 0-3$, $J = 0$), and $b_{max} = 1.0$ a_0. Our motivation for this procedure was first to sample the surface over a wide range of energies based on high-energy collisions involving NH($v = 4$, $J = 10$) and then to refine the surface for higher accuracy using lower energy collisions with NH($v = 0-3$, $J = 0$).

Figure 1 shows how the NH + H reactive cross sections for trajectories initiated with NH($v = 4$, $J = 10$), $E_T = 31.4$ kcal/mol and for NH($v = 0$, $J = 0$), $E_T = 12.6$ kcal/mol varied as the number of data points defining the NHH PES was increased. These cross sections refer to $b_{max} = 4.5$ a_0, which is a large enough maximum impact parameter that it should yield converged reactive cross sections. A total of 5000 trajectories were used for each point in the figure. The figure shows that the cross sections were well converged for 110 or more points. We also found that the number of trajectories, which exhibited poor energy conservation due to an insufficiently smooth surface was negligible for more than about 90 points. Thus we see that roughly 100 points with gradients and Hessians are sufficient to generate a converged surface with the GROW program. The complete set of 156 data points in a format compatible with the GROW program is available in the Supporting Information.

B. Quasiclassical Trajectory Calculations. Standard QCT methods were employed to study the $N(^4S) + H_2$ reaction on the quartet surface. For the ground H_2 vibrational state ($v_{HH} = 0$), a b_{max} of 3.0 a_0 was used for translational energies below 37.7 kcal/mol, increasing to 4.5 a_0 at higher energies (up to 125.5 kcal/mol). For $v_{HH} = 1$, 2, and 3, b_{max}'s of 3.5, 4.0, and 4.0 a_0 were used, respectively. Likewise, the b_{max} values utilized for both (R−1) and (R2) initiated at $v_{NH} = 0$ are 4.0 and 4.5 a_0, for E_T lower and higher than 5.6 kcal/mol, respectively. For $v_{NH} = 1$, 2, 3, and 4, b_{max}'s of 5.5, 6.0, 6.5, and 7.5 a_0 were used, respectively. These b_{max} values were carefully tested with respect to the convergence of cross sections. The initial atom−diatom separation was chosen to be 10.0 a_0 for all calculations. The built-in velocity-Verlet algorithm of GROW was used for the trajectory propagation, using a time step of 0.01 fs. Energy was conserved to typically six figures using this approach on the interpolated surface.

The present study has considered H_2 initial states $v = 0$ ($J =$ 0, ..., 15), $v = 1$ ($J = 1$, ..., 10), and $v = 2, 3$ (all at $J = 0$) for $E_T = 12.6-125.5$ kcal/mol for the forward reaction. For the reverse, and exchange reactions, we considered NH initial states at $v = 0$ ($J = 0$, ..., 20), $v = 1$ ($J = 1$, ..., 10), and $v = 2, 3, 4$ (all at $J = 0$), and $E_T = 0.4-37.7$ kcal/mol. A total of 10 000 trajectories were evaluated for each E_T, and each rovibrational reagent state. For (R1), zero point energy (ZPE) violation is important for $v = 0$, so we have omitted those trajectories that violate ZPE in calculating cross sections.

Additional data required to simulate the diatom vibrational properties in the QCT calculations are the Morse parameters, which include the diatomic equilibrium bond distance (R_e), depth of the potential minimum (D_e), and bond distance prefactor (β). To ensure a close agreement with the NHH PES of this study, the NH and H_2 Morse potential functions were fitted to their corresponding potential energy curves calculated at the MRMP2-(7,6)/6-311++G** level. This procedure led us to the following values for H_2: $R_e = 1.411\ a_0$, $D_e = 0.161744$ au, and $\beta =$ 1.12985 a_0^{-1}. For NH: $R_e = 1.981\ a_0$, $D_e = 0.12394$ au, and β = 1.24674 a_0^{-1}. These values were included in the input data for the standard QCT calculations.

C. Thermal Rate Constant Calculations. The thermal rate constant expression is given by

$$k(T) = Q_{AB}^{-1}\sum_{J_{AB}}(2J_{AB} + 1)(2/k_bT)^{3/2}(\pi\mu)^{-1/2} \times \int_{E_o}^{\infty}\sigma(E_t,J_{AB})e^{-E_t/k_bT}E_t\,dE_t \quad (1)$$

where Q_{AB} is the AB rotational partition function, J_{AB} is the rotational state of AB diatom, μ is the reduced mass of N + H_2 (or H + NH), k_b is the Boltzmann constant, and T is the temperature. Usually, the cross sections $\sigma(E_T,J_{AB})$ were fit via least squares to linear functions of E_T, and then J_{AB} and the resulting fit were used to calculate rate constants through numerical integration of eq 1. In the present study, the calculated cross sections at various J states expressed as a function of E_T, are fit to an exponential function given by

$$\sigma(E_T) = \sigma_\infty - \sigma_\infty \exp[-\beta(E_T - E_o)] \quad (2)$$

where E_o is the threshold energy, σ_∞ is the asymptotic value of the cross section at very high E_T, and β is the energy prefactor. Rearranging this expression and taking the natural logarithm will give us a linear expression, $\ln[\sigma_\infty - \sigma(E_T)] = \ln(\sigma_\infty) + \beta(E_o - E_T)$, which can be used to determine the β, σ_∞, and E_o parameters. Substituting eq 2 into eq 1 and taking the integral equivalent give us an analytical expression for the rate constant:

$$k(T) = Q_{AB}^{-1}\sum_{J}(2J + 1)(2/k_bT)^{3/2}(\pi\mu)^{-1/2} \times \sigma_{\infty J}\left[1 + \frac{E_{oJ}}{k_bT} - \frac{1}{1 + \beta_J k_b T}\left(\frac{1}{1 + \beta_J K_b T} + \frac{E_{oJ}}{k_b T}\right)\right]e^{-E_{oJ}/k_bT} \quad (3)$$

where E_{oJ}, $\sigma_{\infty J}$, and β_J are the usual expressions stated above that are calculated for various reagent J states.

D. Variational Transition State Theory Calculations. We also calculated transition state theory (TST) rate constants using the POLYRATE package of programs,[19] with improved canonical variational theory (ICVT). This method minimizes the microcanonical rate constants along the minimum energy path (MEP) for energies above the threshold, while using the canonical rate constant for energies below threshold. A full description of this method is described elsewhere.[20] Despite the approximations involved, VTST is probably the most used technique to calculate thermal rate constants and it has often been demonstrated that it provides rate constants that agree well (within 20%) with highly accurate quantum dynamics results. For example, in very recent calculations for the benchmark OH + $H_2 \rightarrow H + H_2O$ reaction, VTST results[21a] were found to be in very good agreement with full-dimensional time-dependent calculations (restricted to $J = 0$),[21b] and using the WSLFH PES.[12a] Moreover, VTST provides an excellent alternative to quasiclassical trajectory calculations, as it is able to circumvent the well-known deficiencies associated with classical mechanics. While tunneling is not important for this system at the temperatures where experiments are available, zero point energy leakage associated with QCT is eliminated in the VTST calculations. Recrossing is, however, one flaw associated with VTST calculations, and this is especially important at high temperatures. However, the microcanonical treatment for energies above the threshold (used in ICVT) has been demonstrated to help in the minimization of recrossing effects.[20]

There is one caveat associated with the VTST calculations. Because of the Shepard interpolation representation of the surface, numerical calculation of the second derivatives along the minimum energy reaction path (MEP) often shows ill-defined frequencies in some points. This is due to the fact that in the numerical differencing process, points that do not belong to the MEP have nonzero weight in the interpolation scheme. To avoid this, we have restricted the MEP calculations to points where the frequencies are well-defined, and thus the adiabatic energy curve is smooth.

III. Results and Discussion

A. Stationary Points and Potential Energy Surface. The geometric parameters and vibrational frequencies of the NH and H_2 diatoms optimized at various levels of theory are listed in Table 1. It is evident from this table that both polarization functions and electron correlation are important in the geometry optimization. Notice that without electron correlation, optimized bond lengths are tighter and vibrational frequencies are larger and that electron correlation makes these values longer and smaller, respectively. Likewise, we can also observe a marked improvement of the UHF geometries if we use a multiconfiguration SCF type of calculation. Both UMP2 and UMP4 calculations presented in the table gave excellent agreement of bond length with experiment, but with larger harmonic frequencies. Although the QCISD(TQ)/cc-pVTZ model generated vibrational frequencies that are in good agreement with experiment, it produced the longest bond distance values for both diatoms, among the level of theories presented. We can also observe from Table 1 that the combination of FORS-MCSCF and MCQDPT2 with the 6-311++G** basis set also gives bond length values comparable to the experiment.

Table 2 lists the geometric parameters and frequencies of two linear transition state structures (TSS) that correspond to the abstraction and exchange reactions optimized for various ab initio models. From this table, it can be observed that there is basically the same effect from basis set and electron correlation for the TSS as observed in the reactant and product diatoms. The geometric parameters and frequencies calculated at the FORS-MCSCF(7,6)/6-311++G** level have a quality that is intermediate between the UHF and UMP calculated values. We

TABLE 1: Optimized Bond Distance and Vibrational Frequency of NH and H_2 Diatoms

	$NH(X^3\Sigma^-)$		H_2	
	R_{NH} (Å)	ω (cm^{-1})	R_{HH} (Å)	ω (cm^{-1})
UHF/6-31G[a]	1.032	3372	0.730	4640
UHF/6-311G** [a]	1.023	3501	0.736	4594
HF/cc-pVDZ	1.031	3478	0.748	4579
MP2/6-311G**	1.035	3388	0.738	4533
MP2/6-311++G**	1.035	3395	0.738	4532
MP2−FC/cc-pVDZ	1.046	3343	0.755	4498
MP4/6-311G** [a]	1.042	3295	0.742	4454
MP4SDTQ-FC/6-311++G**	1.041	3307	0.742	4456
MP4SDTQ-FC/cc-pVDZ	1.053	3250	0.759	4418
FORS-MCSCF(7,6)/6-311++G**	1.050	3141	0.757	4224
CASSCF(7,6)/6-311++G**	1.050	3153	0.757	4225
CASSCF(7,6)/cc-pVDZ	1.058	3117	0.770	4210
CASSCF(7,6)/cc-pVTZ	1.047	3148	0.755	4228
CASSCF(7,7)/6-311++G**	1.049	3142	0.757	4225
CASSCF(7,7)/cc-pVDZ	1.059	2996	0.770	4210
CASSCF(7,7)/cc-pVTZ	1.047	3165	0.755	4229
QCISD(T)/6-311++G**	1.044	3256	0.743	4424
QCISD(T)/cc-pVDZ	1.056	3198	0.761	4383
QCISD(T)/cc-PVTZ	1.039	3265	0.743	4410
QCISD(TQ)/cc-pVDZ	1.056	3191		
QCISD(TQ) /cc-pVTZ[b]	1.054	3218	0.761	4384
MRMP2(7,6)/ 6-311++G** [c]	1.048	3292	0.747	4379
expt				
ref 26	1.036	3282	0.741	4401
ref 27	1.036	3282	0.742	4410

[a] Reference 10. [b] Reference 9. [c] Vibrational frequencies were calculated by normal-mode analysis of the optimized structure.

also note that both the geometry and energy values optimized using FORS-MCSCF of GAMESS are basically similar to the CASSCF values of Gaussian 98. When dynamical electron correlation is included in the FORS-MCSCF optimized orbitals, the bond distances of the H1−H2−N3 TSS optimized at MRMP2(7,6)/6-311++G** improved greatly and were in very close agreement with QCISD(TQ)/cc-pVTZ.

The potential barriers and heat of reactions of the forward, reverse, and exchange reactions are listed in Table 3. This table shows improvement in the calculated barriers and heat of reaction as electron correlation is added that is similar to the improvement in the calculated geometric parameters and frequencies of the equilibrium structures. Increasing the basis set size in the CASSCF calculations does not improve the geometric parameters and energy values of the structures much, which implies the sufficiency of 6-311++G** in modeling the reaction. Similarly, the addition of one more unoccupied molecular orbital in the reference MO's of the CASSCF calculation does not show much improvement to the geometrical parameters and energies, which suggests the sufficiency of including the first unoccupied N−H antibonding MO only in the CASSCF calculations. Among the single reference calculations compared, the QCISD calculations give the best agreement with experiment for the energy barrier of (R1). In the QCISD(T) calculation, there is also a small change to both geometry and energy values when the basis set size is increased from 6-311G** to 6-311++G**, but QCISD(TQ) using a cc-pVTZ basis set gives the best estimate for the energy barrier of (R1) at 29.6 kcal/mol. Similarly, better agreement with the experiment is realized if we add dynamical electron correlation to the FORS-MCSCF result. The MRMP2(7,6)/6-311++G** model does this type of calculation and the optimized geometric parameters, frequencies, and energies at this level show excellent agreement with the experiment and other high-level ab initio calculations, particularly the QCISD(TQ)/cc-pVTZ model. For the reverse reaction (R−1), we can also see from Table 3 that the MRMP2(7,6)/6-311++G** calculated geometric parameters and energy barrier show excellent agreement with those predicted by other high-level ab initio methods. The qualities of the MRMP2(7,6)/6-311++G** ab initio model provide a good indication of its sufficiency for more rigorous PES development and QCT calculations.

TABLE 2: Geometric Parameters and Frequencies of Two Transition State Structures (Both Structures Collinear)

	bond distances (Å)		frequencies (cm^{-1})			
	R_{12}	R_{23}	$\omega_1(\sigma)$	$\omega_2(\pi)$	$\omega_3(\pi)$	$\omega_4(\sigma)$
A. H1−H2−N3						
UHF/6-31G[a]	1.203	1.138	2084i	766	766	1319
UHF/6-311G** [a]	1.103	1.154	2450i	797	797	1352
UMP2/6-311G** [a]	1.103	1.130	1748i	824	824	1592
UMP2−FC/6-311G**	1.105	1.130	1747i	815	815	1592
UMP2/6-311++G**	1.136	1.091	1827i	816	816	1564
UMP4/6-311G** [a]	1.190	1.111	1311i	574	602	1773
UMP4SDTQ-FC/6-311G**	1.191	1.111	1237i	720	720	1811
UMP4SDTQ-FC/6-311++G**	1.175	1.115	1287i	722	722	1767
FORS-MCSCF(7,6)/6-311++G**	1.157	1.164	2051i	755	755	1310
CAS(7,6)/6-311++G**	1.158	1.163	2043i	756	756	1316
CAS(7,6)/cc-pVDZ	1.183	1.163	1939i	723	723	1329
CAS(7,6)/cc-pVTZ	1.154	1.163	2060i	752	752	1308
CAS(7,7)/6-311++G**	1.157	1.164	2053i	756	756	1313
CAS(7,7)/cc-pVDZ	1.156	1.169	2173i	556	556	1240
UQCISD(T)/6-311++G**	1.228	1.109	1025i	665	665	1817
UQCISD(TQ)/6-311++G**	1.233	1.109	1006i	660	660	1829
UQCISD(TQ)/cc-pVTZ	1.212	1.109	1022i	694	695	1760
QCISD(TQ)/cc-pVTZ[b]	1.275	1.109	930i	626	626	1919
MRMP2(7,6)/ 6-311++G** [c]	1.273	1.105	963i	631	631	1824
B. H1−N2−H3						
FORS-MCSCF(7,6)/6-311++G**	1.292	1.292	2609i	1057	1057	1667
CAS(7,6)/6-311++G**	1.293	1.293	2629i	1057	1057	1663
CAS(7,6)/cc-PVDZ	1.319	1.319	2610i	1039	1039	1671
CAS(7,6)/cc-PVTZ	1.233	1.233	3091i	1159	1159	2091
UQCISD(T)-FC/6-311++G**	1.246	1.246	2017i	1040	1040	1842
UQCISD(TQ)-FC/6-311++G**	1.248	1.248	2003i	1038	1038	1831
UQCISD(T)/cc-pVTZ	1.259	1.259	2158i	1075	1076	1868
UQCISD(TQ)/cc-pVTZ	1.260	1.260	2158i	1076	1076	1868
MRMP2(7,6)/6-311++G** [c]	1.254	1.254	1589i	1031	1031	1822

[a] Reference 10. [b] Reference 9. [c] Vibrational frequencies were calculated using a normal-mode analysis.

Figure 2 presents a contour plot of the interpolated NH_2 potential for a fixed NH distance of 2.2 a_0, as a function of the H atom's (x, y) coordinates. This contour clearly shows the collinear nature of the TSS that corresponds to (R1). The configuration of the barrier is consistent with other high-level ab initio studies,[10,11] which also optimized a collinear N−H−H transition structure for (R1). Also notice that the potential is repulsive perpendicular to the NH bond; this precludes the presence of any insertion mechanism for either abstraction or exchange reactions. Aside from being collinear, we can observe from Figure 3 that the reaction has a late, and early barrier with respect to (R1) and (R−1), respectively. The late barrier characteristic of (R1) is also supported by the ab initio study of Zhang and Truong, where they plotted the NH and H_2 bond lengths vs the mass weighted internal coordinate s along the intrinsic reaction coordinate (IRC) path of the reaction. They found that the energy rises sharply in the region where the H−H bond is breaking up prior to the saddle point, whereas the N−H bond is still in the process of forming. They added that at the transition state, the N−H bond is already 95% formed.

B. Forward Reaction, $N(^4S) + H_2 \rightarrow NH(X^3\Sigma^-) + H$. Table 4 summarizes cross sections and the product state distribution information for the three reactions considered in this study. Included in this table are the initial and final relative translational and rovibrational energies (E_T and E_{vJ}) and ($\langle E'_T\rangle$ and $\langle E'_{vJ}\rangle$), the total cross section Q_{react}, the normalized vibrational distribution, the average vibrational quantum number $\langle v'\rangle$, and rotational quantum numbers $\langle J'\rangle$ for each v', and the average product scattering angle $\langle\theta\rangle$. Statistical uncertainties in the table are roughly $\pm 0.06\ a_0^2$ in the cross section, ± 0.01 in vibrational population, ± 0.04 in $\langle v\rangle$, ± 1 in $\langle J\rangle$, ± 0.05 in $\langle\theta\rangle$. In the

TABLE 3: Potential Barriers and Energies of Reaction (kcal/mol) in the NHH PES Calculated at Various Levels of Theory

	forward barrier		reverse barrier		reaction energy	
	ΔE_o	ΔE_{ZPE}[a]	ΔE_o	ΔE_{ZPE}[a]	ΔE_o	ΔE_{ZPE}[a]
A. N(^{4}S) + H_2 ↔ NH(X^{3}S$^-$) + H						
UHF/6-311G**	43.7	41.3	9.4	8.6	34.3	32.7
UMP2/6-311G**	35.1	33.3	5.5	5.3	29.6	28.0
UMP2/6-311++G**	34.3	32.3	5.8	5.5	28.5	26.9
UMP4SDTQ/6-311G**	35.6	33.9	3.6	3.5	32.0	30.4
UMP4SDTQ/6-311++G**	34.6	32.8	3.7	3.6	30.9	29.2
MP−SAC4/6-311G** [b]	32.1	30.2	1.9	1.7	30.2	28.6
FORS-MCSCF(7,6)/6-311++G**	39.0	36.7	7.8	7.4	31.1	29.4
CAS(7,6)/6-311++G**	39.0	37.0	7.9	7.4	31.1	29.6
CAS(7,6)/cc-pVDZ	38.9	36.8	7.0	6.5	31.8	30.3
CAS(7,6)/cc-pVTZ	39.0	36.9	7.9	7.4	31.0	29.5
CAS(7,7)/6-311++G**	39.0	37.0	7.9	7.4	31.1	29.6
CAS(7,7)/cc-pVDZ	37.1	34.4	7.3	6.4	29.7	28.0
UQCISD(T)/6-311G** [b]	34.0		2.2	2.0	31.9	30.2
UQCISD(T)/6-311++G**	33.1	31.3	2.4	2.3	30.7	29.0
QCISD(TQ)/cc-pVTZ[c]	31.3	29.6	2.2	0.5	29.2	29.1
MRMP2(7,6)/6-311++G**	32.4	30.2	2.4	1.9	30.1	28.3
expt[d]		25.1		0.3		24.3
other expt		33 ± 7[e]		1.5[f]		20.1[f]
B. H + NH(X^{3}S$^-$) → HN (X^{3}S$^-$) + H						
FORS-MCSCF(7,6)/6-311++G**	31.6	32.6	31.6	32.6	0.0	0.0
UQCISD(T)/6-311++G**	22.9	23.9	22.9	23.9	0.0	0.0
UQCISD(T)/cc-pVTZ	23.4	24.5	23.4	24.5	0.0	0.0
UQCISD(TQ)/6-311++G**	22.8	23.7	22.8	23.7	0.0	0.0
MRMP2(7,6)/6-311++G**	22.1	23.0	22.1	23.0	0.0	0.0

[a] ZPE corrected energies. [b] Reference 10. Single-point calculations at UMP2/6-311G** geometry. [c] Reference 9. [d] Reference 5. Barriers are estimated from Arrhenius activation energy. [e] Reference 4. [f] Reference 26.

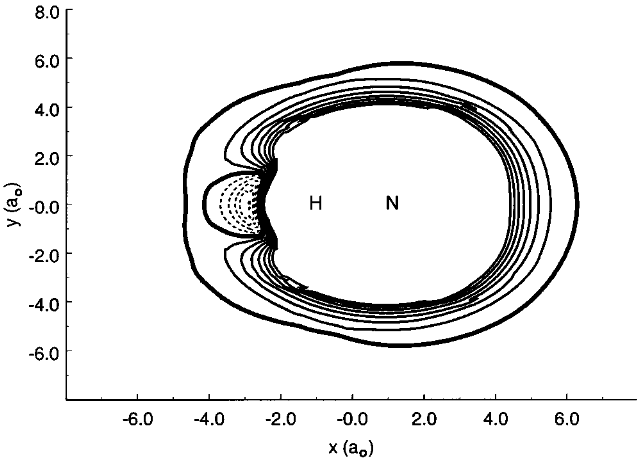

Figure 2. Contour plot of the NHH potential as a function of the *x*, *y* location of H atom. The NH bond distance is fixed at 2.2 a_0 and oriented along the *x* axis. Contours are spaced by 1 kcal/mol where dashed contours indicate decreasing potential energy, with the bold solid contour as the reference point. Thinner solid contours indicate increasing potential energy.

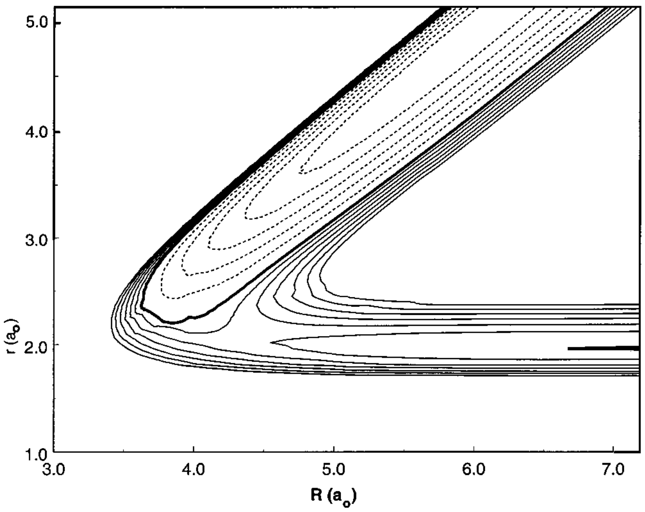

Figure 3. Contour plot of the NHH potential for fixed linear configuration. The potential is plotted as a function of the Jacobi coordinate *R* and the NH distance. Contours are spaced by 2 kcal/mol for positive energy contours (solid curves), and 5 kcal/mol for negative energy contours (dashed curves). The zero of energy is defined as NH(X$^3\Sigma^-$) + H at equilibrium, and the zero contour is indicated by the thick solid line.

following discussion, we examine the information in this table, along with other figures and tables, for the three reactions.

1. Integral Cross Section. Figure 4a presents the integral cross section as a function of reagent kinetic energy for (R1) initiated with $v = 0$ and $J = 0{-}15$ on the interpolated MRMP2(7,6)/6-311++G** surface. For lower H_2 rotational states, the figure shows that the cross section has an interpolated threshold energy of 42.7 kcal/mol at $J = 0$ and gradually decreases with increasing J to 22.6 kcal/mol at $J = 15$ (see Table 5 for the fitted E_o). Above the threshold energy, the cross section for $J = 0$ rises almost linearly up to 80 kcal/mol, then bends over at 100 kcal/mol, and increases slowly up to 125 kcal/mol. Higher rotational states show a steeper initial linear rise, bending over earlier, and reaching larger cross sections. At $J = 15$, the steep linear rise of the cross section just above threshold is noticeable, then the excitation function bends at 50−80 kcal/mol, reaching a broad peak at $E_T = 100$ kcal/mol, before noticeably dropping at higher E_T. A similar trend of decreasing threshold energy is also observed for $v_{HH} = 1$ as J_{HH} is increased (see Table 5). Like most endoergic triatomic reactions with a late barrier, there is a significant increase in reactivity with increasing reagent vibrational excitation. This behavior is clearly observed in Figure 4b, where the threshold energy dramatically decreases and the slope of the excitation function increases as the vibrational excitation of the reagent H_2 is increased. The shape of the cross section curves presented in Figure 4 is similar to what is generally observed for all reactions that possess potential energy barriers.[11,22,24]

2. Vibrational, Rotational, and Angular Distribution. Figure 5 shows the final vibrational distribution for (R1) at $E_T = 37.7$

TABLE 4: Trajectory Results for Forward (R1), Reverse (R−1), and Exchange Reactions (R2) with Specified Initial Translational Energies, E_T (kcal/mol), and $v = 0$, and $J = 0$ Reagent States

	R1		R−1			R2
E_T	37.7	56.5	3.8	12.6	31.4	31.4
E_{vj} ($v = 0, J = 0$)	6.5	6.5	4.6	4.6	4.6	4.6
$\langle E'_T \rangle$	9.7	21.8	20.6	28.6	41.0	29.1
$\langle E'_{vj} \rangle$	4.4	11.1	17.9	18.6	25.1	7.0
Q_{react} (a_0^2)	0.40	2.50	2.50	4.50	5.48	0.40
vib dist'n[a]						
$v' = 0$	0.99	0.86	0.28	0.51	0.69	0.81
$v' = 1$	0.01	0.17	0.72	0.44	0.20	0.17
$v' = 2$	0.001	0.02	0.001	0.04	0.07	0.02
$v' = 3$		0.001		0.003	0.03	
$v' = 4$					0.004	
$v' = 5$					0.001	
$\langle v' \rangle$	0.00	0.07	0.70	0.46	0.41	0.13
av J's						
$\langle J' \rangle_{v'=0}$	6	11	4	6	9	4
$\langle J' \rangle_{v'=1}$	3	9	3	5	7	3
$\langle J' \rangle_{v'=2}$	1	8	0	3	6	1
$\langle J' \rangle_{v'=3}$		9		2	5	
$\langle J' \rangle_{v'=4}$					5	
$\langle J' \rangle_{v'=5}$					3	
$\langle J' \rangle_{all\,v'}$	6	10	3	5	8	4
av θ's						
$\langle \theta \rangle_{v'=0}$	2.19	2.00	2.24	2.09	1.77	2.54
$\langle \theta \rangle_{v'=1}$	2.37	1.92	2.35	2.05	1.85	2.49
$\langle \theta \rangle_{v'=2}$	2.52	1.90	2.84	2.16	1.71	2.52
$\langle \theta \rangle_{v'=3}$		2.58		2.16	1.76	
$\langle \theta \rangle_{v'=4}$					1.83	
$\langle \theta \rangle_{v'=5}$					1.83	
$\langle \theta \rangle_{total}$ (rad)	2.19	1.99	2.32	2.07	1.78	2.53

[a] Normalized to unity.

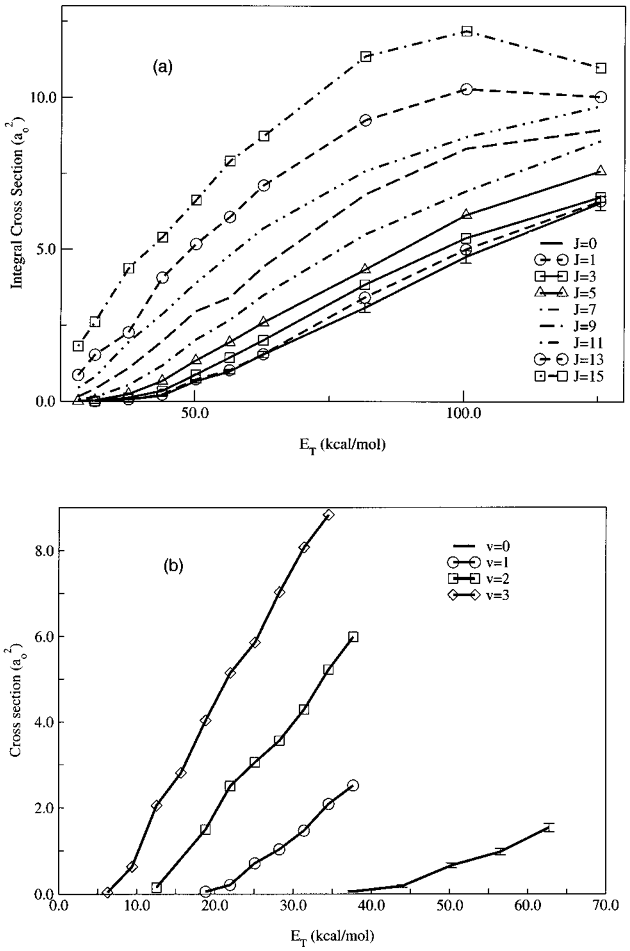

Figure 4. (a) Integral cross section as a function of reagent translational energy for (R1), with the H_2 initial states being ($v = 0$, $J = 0$, 15). (b) Same information but the H_2 diatom is in $J = 0$, while initial vibrational states are varied from 0 to 3. A representative error bar is given for trajectories initiated at $v = 0$, $J = 0$ states.

and 56.5 kcal/mol, for $v = 0$, $J = 0$. We can see from this figure and from Table 4 that the vibrational distribution is dominated by the ground state and is generally a monotonically decreasing function of v. In addition, a slow increase can be observed in the average vibrational excitation with increasing reagent translational energy. Shown in Figure 6 is the product state rotational distribution as a function of the NH J' quantum number for $v' = 0$, 1. This figure and Table 4 show that rotational excitation is very high for $v' = 0$, and considerably drops for $v' = 1$. In addition, rotational excitation increases with increasing E_T of the reagents. At $E_T = 37.7$ kcal/mol, for instance, the NH rotational distribution for $v' = 0$ peaks at about $J' = 5$ with a cross section of 0.06 a_0^2. This peak shifts toward $J' = 13$ with a corresponding increase in cross section ($Q_{react} = 0.18\ a_0^2$) when the $E_T = 56.5$ kcal/mol. Although there are not enough reactive trajectories for $E_T = 37.7$ kcal/mol to determine statistically meaningful rotational distributions for NH $v' = 1$, a broad curve that peaks at $J' = 9$ is observed when $E_T = 56.5$ kcal/mol.

Figure 7 presents the differential cross section as a function of scattering angle (the angle between the reagent atom velocity and the product diatom velocity) for (R1) initiated at $v = 0$, $J = 0$, and $E_T = 37.7$ and 56.5 kcal/mol. For both energies, the product angular distribution of the NH diatoms is backward peaked. This behavior is what is expected for reactions that have collinear transition state structures, particularly A + XH reactions, where A = H, D, Cl, Br, I, and O (^{1}D on 1A″ surface) and X = H, D.[13,22,23] There is also a noticeable shifting of the distribution to sideward scattering, as the relative translational energy of the reaction increases. The calculated average scattering angles also reflect this shift, with values of 125° and 114° for $E_T = 37.7$ and 56.5 kcal/mol, respectively (see Table 4).

3. Thermal Rate Constants. Listed in Table 5 are fitting parameters derived from eq 2 for the reactive cross sections for various initial H_2 rovibrational states. These parameters were used in calculating the Boltzmann J-state averaged thermal rate constant of (R1) using eq 3. In Figure 8, we can see that the QCT-derived rate constant is noticeably higher but otherwise in good agreement with the values observed by Davidson and Hanson[5] and Koshi et al.,[4] and as calculated by Zhang and Truong.[9] An Arrhenius expression that fits closely to the present results is $k(T) = 6.85 \times 10^{-10} \exp(-25.9(\text{kcal/mol})/RT)$ cm^3 molecule^{-1} s^{-1}. Here the calculated activation energy closely agrees with the experimental estimate, 25.1 kcal/mol, as determined by Davidson and Hanson.[5] However, both Koshi et al.,[4] and Zhang and Truong,[9] give larger activation energies, which they reported as 33 ± 7 and 30.8 kcal/mol, respectively. On the other hand, the preexponential factor for this expression is more than twice as large as that derived by Davidson and Hanson[5] (2.7×10^{-10}), and a little larger than the value derived by Koshi et al.[4] ($(4.6 \pm 0.3) \times 10^{-10}$) and Zhang and Truong[9] (3.87×10^{-10}).

Figure 8 also presents the ICVT rate constant. This result is below the QCT result but is in good agreement with experiments in the temperature range where experiments are available. The fitted Arrhenius expression for the ICVT result is $k(T) = 5.52 \times 10^{-10} \exp(-32.4(\text{kcal/mol})/RT)$ cm^3 molecule^{-1} s^{-1}. There is a good match with the previous VTST predictions of VTST rate constants by Zhang and Truong, who used limited ab initio points along the MEP for their calculations. The difference between the QCT and ICVT results could arise either from zero

TABLE 5: Fitting Parameters Needed in Eq 2 for Representing the Actual Reactive Integral Cross Sections of (R1) As Initiated at $v_{HH} = 0$, $J_{HH} = 0-15$ and $v_{HH} = 1$, $J_{HH} = 0-10$

	$v = 0$			$v = 1$		
J_{HH}	E_o (kcal/mol)	σ_∞ (a_0^2)	β [1/(kcal/mol)]	E_o (kcal/mol)	σ_∞ (a_0^2)	β [1/(kcal/mol)]
0	42.67	55.00	0.0015	21.96	15.00	0.0092
1	40.79	35.00	0.0026	21.96	15.00	0.0093
2	40.79	55.00	0.0016	21.96	15.00	0.0095
3	40.16	18.00	0.0057	21.96	13.00	0.0127
4	37.02	25.00	0.0038	20.08	13.00	0.0129
5	35.77	20.00	0.0055	18.20	12.50	0.0155
6	33.26	22.00	0.0051	18.20	12.00	0.0181
7	30.75	20.00	0.0061	16.94	13.00	0.0180
8	29.49	16.00	0.0088	16.32	13.00	0.0210
9	27.61	26.00	0.0055	15.69	13.00	0.0242
10	26.36	20.00	0.0075	15.06	12.40	0.0320
11	26.36	12.00	0.0173			
12	25.73	12.90	0.0187			
13	25.10	14.00	0.0183			
14	24.47	12.90	0.0269			
15	22.59	15.00	0.0223			

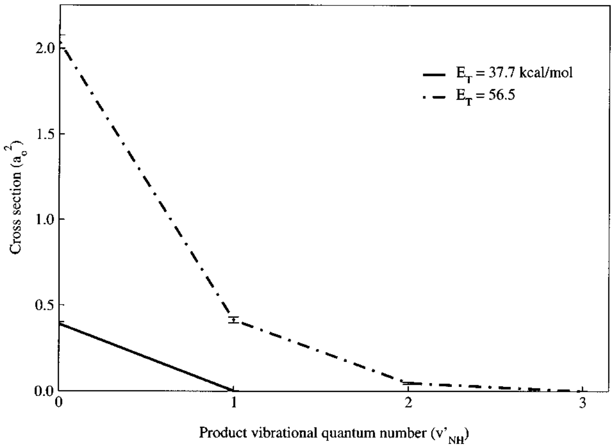

Figure 5. Vibrational distribution for the N + H_2 reaction, plotted as integral cross section vs product (NH) vibrational quantum number for trajectories initiated with E_T = 37.7, and 56.5 kcal/mol, v = 0, and J = 0.

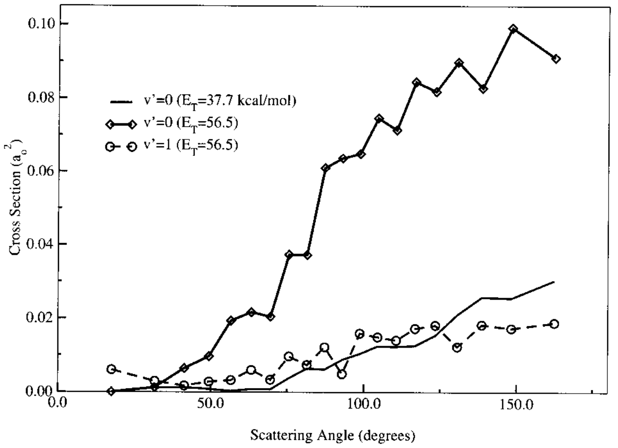

Figure 7. Differential cross section vs scattering angle θ for the N + $H_2 \rightarrow$ NH + H reaction, resolved into final vibrational states of NH. Initial QCT conditions were E_T = 37.7 and 56.5 kcal/mol, v = 0, and J = 0.

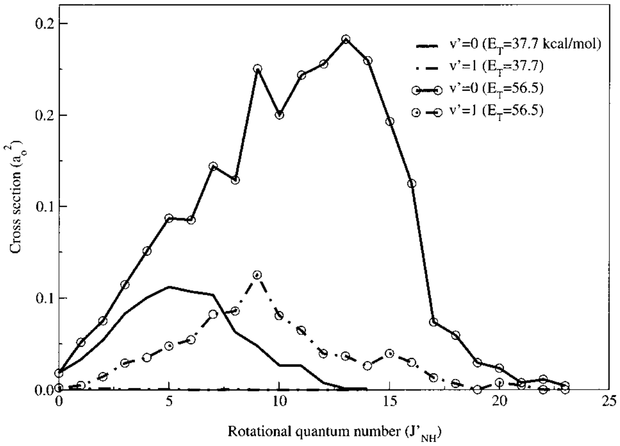

Figure 6. Rotational distribution for the N + H_2 reaction, plotted as integral cross section vs product (NH) rotational quantum number J with E_T = 37.7, and 56.5 kcal/mol, v = 0, and J = 0.

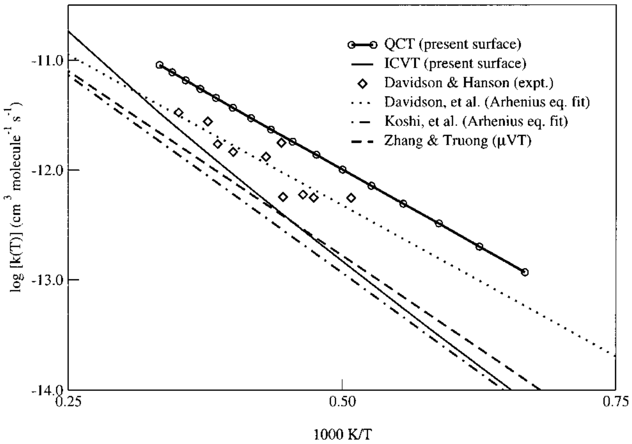

Figure 8. Arrhenius plot of the thermal rate constant of N(^{4}S) + H_2 $\rightarrow$ NH($X^3\Sigma^-$) + H reaction.

point energy violations in the QCT calculations (this can occur even though we imposed a zero point constraint in the cross section calculation) or from anharmonic effects in the high-temperature partition functions that are not considered in our VTST treatment.

C. Reverse Reaction, NH($X^3\Sigma^-$) + H $\rightarrow$ N(^{4}S) + H_2. *1. Integral Cross Section.* Figure 9a presents the integral cross section as a function of reagent kinetic energy for the reverse reaction with $v = 0$ (J = 0, 2, 4, 6, 8, 10, 15, 20) initial states. Unlike the forward reaction, the figure shows that the cross section has a threshold energy that noticeably increases with increasing initial J. In Table 6, we can see that at J = 0, the fitted threshold energy is at its lowest (about 0.4 kcal/mol). It gradually increases with J to 2.5 kcal/mol at J = 10−17, before noticeably descending to 1.9 kcal/mol at J = 20. Generally, the cross sections for all J states have an arching shape with a steep initial rise before bending over toward a plateau at about

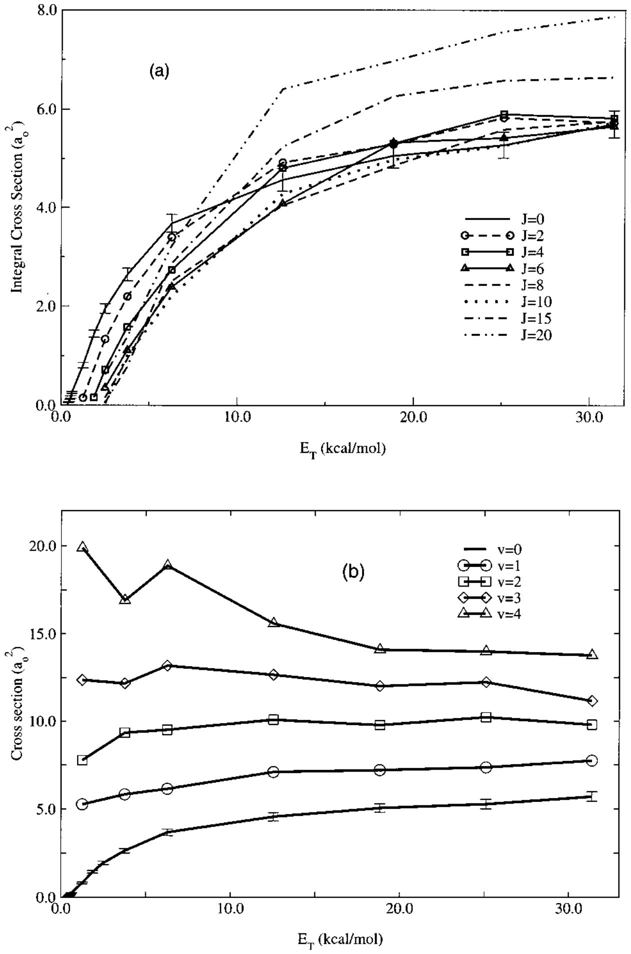

Figure 9. (a) Integral cross section as a function of reagent translational energy for (R−1), with the NH initially having $v = 0$, $J = 0, 2, ..., 10$ with J being even. (b) Same information but the NH diatom is in $J = 0$, with $v = 0-4$. A representative error bar is given for trajectories initiated with $v = 0$, $J = 0$.

25.1 kcal/mol. In addition, the cross section for lower initial J states is noticeably larger at lower translational energy, and the reactive cross section for $J = 7-10$ appears to converge to fairly constant values, and much higher J states ($J = 15, 20$) show increasing reaction cross sections as E_T increases (see Table 6 for the σ_∞ trend). These results suggest that in this reaction rotational excitation of the reagent diatom does not necessarily translate to larger reaction cross sections for the $J = 0-10$ range. This implies that the steric factor is important for this reaction at these reagent diatom J states. For higher J, however, a balance between steric factor and the availability of more energy brought about by rotational excitation is achieved, thus giving "converged" reaction cross sections at least up to $J = 10$. When the J_{NH} state is further increased ($J = 11-20$), the positive effect toward the reaction cross is more prominent at higher E_T, where we observed a corresponding increasing trend. A similar observation but on a different reaction (D + H$_2$), was also observed by Aoiz et al.[24] They found that the cross section for this reaction at $E_T = 8.2$ kcal/mol generally decreases with increasing J from 0 to 3 and remains fairly constant from $J = 3-6$, before rising almost exponentially from $J = 6-10$. A similar result is also observed when we analyzed the effect of increasing the initial J_{NH} for the $v_{NH} = 1$ state on the reaction cross section (see Table 6). Note that the fitted threshold energy is negative for $v = 1$, $J = 0-4$ initial states, which reflects a barrierless reaction. As J_{NH} increases, the threshold energy also increases, while the asymptotic reaction cross section (σ_∞) at high E_T is almost independent of J_{NH} for $J_{NH} = 0-5$ (7.1−7.4 a_0^2) and then gradually increases to 8.9 a_0^2 at $J = 10$.

The effect of reagent vibrational excitation for the present reverse reaction is shown in Figure 9b, which illustrates the absence of threshold energies for all states higher than $v = 0$. The cross sections for $v = 1-3$ are almost independent of E_T, whereas those with $v = 4$ decrease with increasing E_T. This result is common for barrierless reactions. In the present case the potential barrier, being 2.4 kcal/mol, is easily overcome by vibrational excitation. Although this reaction has an early barrier, we can observe a positive increase in the cross section with increasing vibrational excitation, which is in contrast to what is commonly assumed in the Polanyi Rules.[25] This increase can be explained by examining representative reactive trajectories for different vibrational excitation, and the topology of the NHH PES as shown in Figure 10. We can see in this figure that as the vibrational excitation is increased, it will allow the trajectories to reach higher rungs on the PES, which have earlier turning points toward the product. Thus in Figure 10 for $v = 4$, we see that the trajectory is already strongly perturbed at $r_{HH} = 4$, while the lower v's yield perturbed trajectories at successively smaller r_{HH}.

2. Vibrational, Rotational, and Angular Distributions. The reverse reaction is 30.1 kcal/mol exoergic. Table 4 presents product state distribution information for this reaction for three reagent translational energies. This shows that product rovibrational excitation is favored at lower reagent E_T, receiving 46% of the available energy. This reduces to 39% and 38% when reagent E_T is increased to 12.6 and 31.4 kcal/mol, respectively. Conversely, the rest of the available energy is in the form of product translational energy, which increases with increasing reagent E_T.

Figure 11 shows the vibrational distribution for (R−1) initiated at $E_T = 3.8$, 12.6, and 31.4 kcal/mol and $v = 0$, $J = 0$. It shows that at $E_T = 3.8$ kcal/mol, the product (H$_2$) vibrational distribution is dominated by $v' = 1$, which has a cross section that is almost thrice that for $v' = 0$. When $E_T = 12.6$ kcal/mol, the vibrational distribution shifts in favor of $v' = 0$, while the cross section for $v' = 1$ is practically unchanged. Still at higher E_T (31.4 kcal/mol), the vibrational distribution is completely dominated by $v' = 0$, while the cross section for $v' = 1$ drops considerably and higher vibrational states are also populated. This behavior can be explained by observing the trajectories and keeping in mind that this reaction is considerably exoergic. Most trajectories for lower E_T show that relative translation of the reagents is very slow compared to the vigorous ground-state vibration of the NH diatom. Because of the slow H approach, most of the reactive trajectories have the NH bond elongated at the point of atom transfer. The resulting H$_2$ diatom is thus highly excited. At higher E_T, the approaching H can frequently catch the NH diatom in its compressed, relaxed, or stretched state at the point of H transfer, thereby giving a broader distribution among translation, rotation, and vibration. In Figure 12, we can also see how representative trajectories initiated at low and high E_T behave on the NHH PES. For representative trajectories initiated at low E_T (3.8 kcal/mol), H atom transfers when the NH is in its stretched state brings about the vibrational excitation of the product. However, trajectories initiated at $E_T = 31.4$ kcal/mol produce the $v'_{HH} = 0$ state as a result of the attacking H atom catching the NH bond in its compressed state. This configuration leads to a strong rebound of the formed H$_2$ bond, thereby favoring high product translational energy as a form of energy disposal. On the other hand, when a fast trajectory catches the NH diatom in its stretched

TABLE 6: Fitting Parameters Needed in Eq 2 for Representing the Actual Reactive Integral Cross Sections of (R−1) As Initiated at $v_{NH} = 0$, $J_{NH} = 0-20$ and $v_{NH} = 1$, $J_{NH} = 0-10$

	$v = 0$			$v = 1$		
J_{NH}	E_o (kcal/mol)	σ_∞ (a_0^2)	β [1/(kcal/mol)]	E_o (kcal/mol)	σ_∞ (a_0^2)	β [1/(kcal/mol)]
0	0.38	5.32	0.1805	−5.65	7.06	0.1987
1	0.63	5.57	0.1772	−5.02	7.39	0.1598
2	0.94	5.85	0.1607	−2.32	7.35	0.1953
3	1.26	5.86	0.1584	−0.31	7.38	0.2590
4	1.57	6.00	0.1368	0.13	7.08	0.2918
5	1.69	6.01	0.1233	0.31	7.33	0.2933
6	2.01	5.82	0.1219	0.44	7.56	0.3135
7	2.20	5.93	0.1221	0.56	8.20	0.2522
8	2.20	5.95	0.1173	0.82	8.26	0.2871
9	2.38	5.83	0.1326	0.94	8.98	0.2521
10	2.45	5.84	0.1255	1.00	8.90	0.2464
11	2.45	7.24	0.1021			
12	2.45	6.93	0.1187			
13	2.45	6.75	0.1300			
14	2.45	6.92	0.1295			
15	2.45	6.77	0.1471			
16	2.45	7.30	0.1225			
17	2.45	7.51	0.1342			
18	2.20	7.81	0.1242			
19	2.20	7.70	0.1353			
20	1.88	8.05	0.1266			

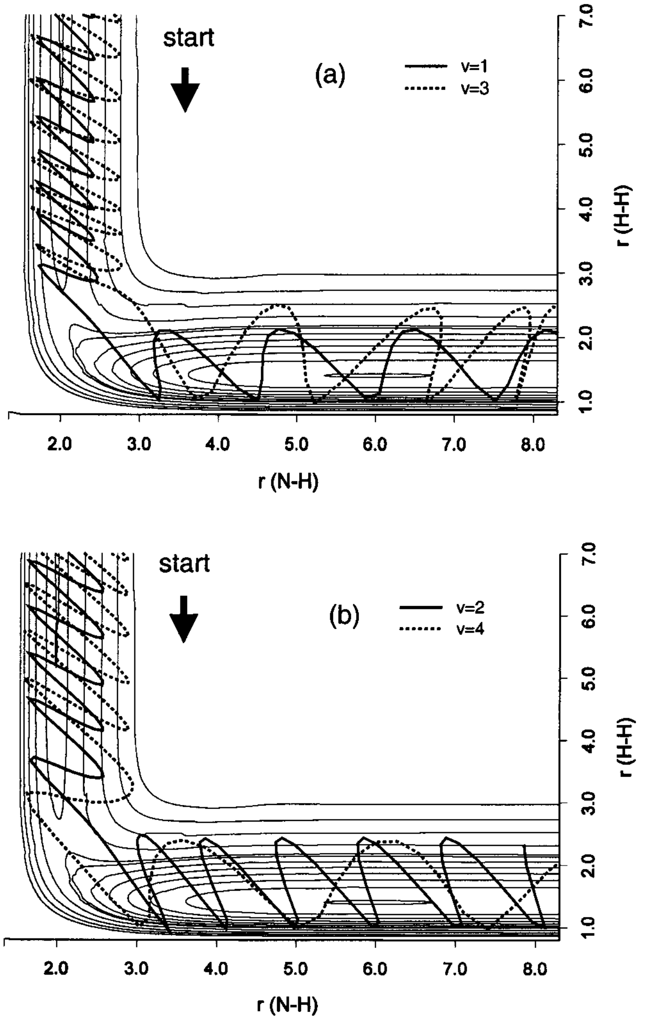

Figure 10. Representative reactive trajectories for (R−1) for NH vibration states $v = 1, 2, 3, 4$, as plotted on the collinear NHH surface. The trajectories are initiated with $E_T = 0.6$ kcal/mol. Bond distances are in atomic units (a_0).

state, this will result in very high product vibrational excitation. Table 4 also summarizes these trends where the average product vibrational states, $\langle v' \rangle$'s, for trajectories initiated at $E_T = 3.8$, 12.6, and 31.4 kcal/mol are 0.70, 0.46, and 0.41, respectively.

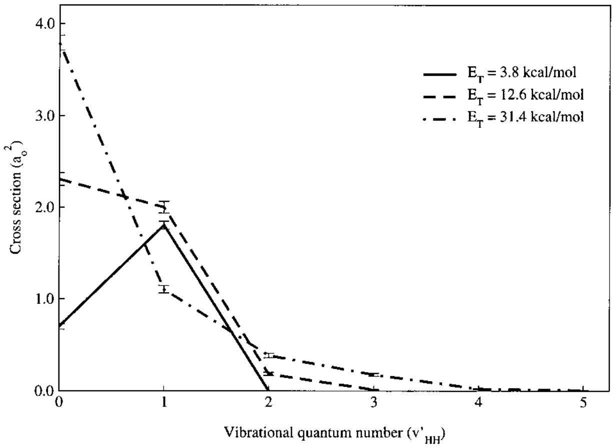

Figure 11. Vibrational distribution for the NH + H reaction, plotted as integral cross section vs product (H_2) vibrational quantum number for trajectories initiated with $E_T = 3.8$, 12.6, and 31.4 kcal/mol, $v = 0$, and $J = 0$.

Figure 13 shows the product rotational distribution for (R−1) initiated at $E_T = 3.8$, 12.6, and 31.4 kcal/mol, $v = 0$, and $J = 0$. The figure shows that the rotational excitation is higher for $v' = 0$ than for $v' = 1$. As with the forward reaction (R1), the rotational excitation increases with increasing reagent E_T. At $E_T = 3.4$ kcal/mol, for instance, the rotational distribution of H_2 with $v = 0$ peaks at about $J' = 4$ with a cross section of 0.16 a_0^2. This peak shifts toward $J' = 7$ and 10, with much larger cross sections (0.40 and 0.46 a_0^2), for $E_T = 12.6$ and 31.4 kcal/mol, respectively. Although the peak J' for $v = 1$ is also increasing, the corresponding cross section decreases as E_T increases.

Figure 14 presents the differential cross section as a function of scattering angle for (R−1) at $v = 0$ and $J = 0$ initial states and $E_T = 3.4$, 12.6, and 31.4 kcal/mol. At lower energies, the product angular distribution of the NH diatom, both with $v = 0$ and $v = 1$ states, is backward peaked. However, at $E_T = 31.4$ kcal/mol, there is a marked broadening of the scattering angle toward the sideways direction, especially for the ground vibrational state. This observation is also reflected in Table 4, where the overall average scattering angles are 133°, 119°, and 102°, for reactions initiated at $E_T = 3.4$, 12.6, and 31.4 kcal/mol, respectively.

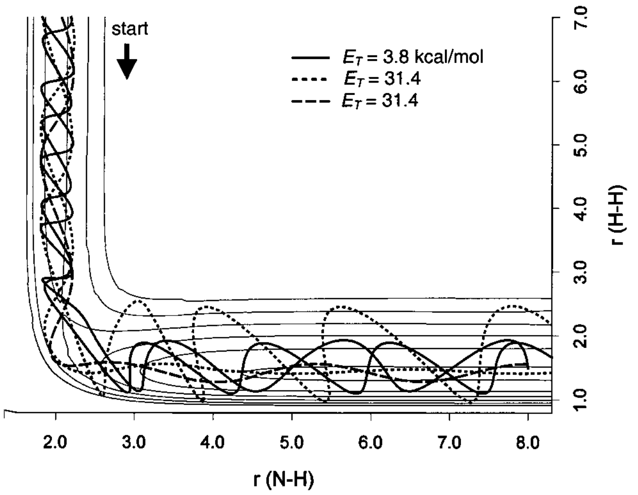

Figure 12. Representative trajectories for (R−1) plotted on the collinear NHH surface showing product vibrational excitation of trajectories initiated at E_T = 3.8, and 31.4 kcal/mol. Bond distances are in atomic units (a_0).

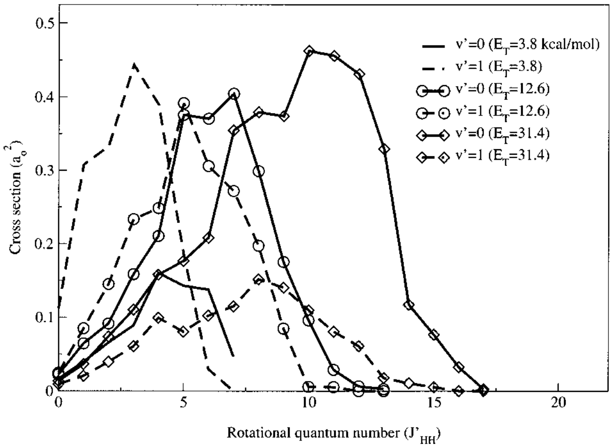

Figure 13. Rotational distribution, plotted as cross section vs product (H_2) rotational quantum number J at E_T = 3.8, 12.6 and 31.4 kcal/mol for (R−1) initiated at v = 0 and J = 0.

3. Thermal Rate Constants and ICVT Calculation. Listed in Table 6 are the parameters used in eq 2 to represent the reaction cross sections for various initial NH rovibrational states. Contributions from v_{NH} = 1 vary from 1 to 17% in the temperature range 1000−2500 K; hence the fitted parameters for various J_{NH} states were also derived. As with the forward reaction, these parameters were used in calculating the Boltzmann J-state averaged thermal rate constant using eq 3. In calculating the rate constant we have multiplied the cross sections by the electronic degeneracy factor ($^2/_3$) associated with reaction on the quartet state.

In Figure 15, we can see that the QCT rate constant closely agrees with the experimental value as observed by Davidson and Hanson, and with those calculated by Zhang and Truong and Fu et al. in the temperature range 2000−3000 K. The calculated QCT rate constant can be expressed in the Arrhenius form as $k(T) = 1.85 \times 10^{-14}T^{1.07} \exp(-2.2(\mathrm{kcal/mol})/RT)$ cm^3 molecule^{-1} s^{-1}. The ICVT k_{-1} rate constant, also plotted in Figure 15, is likewise in good agreement with the experimental measurements. This can be expressed as $k(T) = 1.56 \times 10^{-16}T^{1.64} \exp(-0.7(\mathrm{kcal/mol})/RT)$ cm^3 molecule^{-1} s^{-1}. It is noticeable that the agreement with the earlier VTST calculations of Zhang and Truong is better than the agreement between the two sets of experiments. This is likely an indication that both calculations are essentially correct and that the experimental uncertainty associated with the experiments is relatively large.

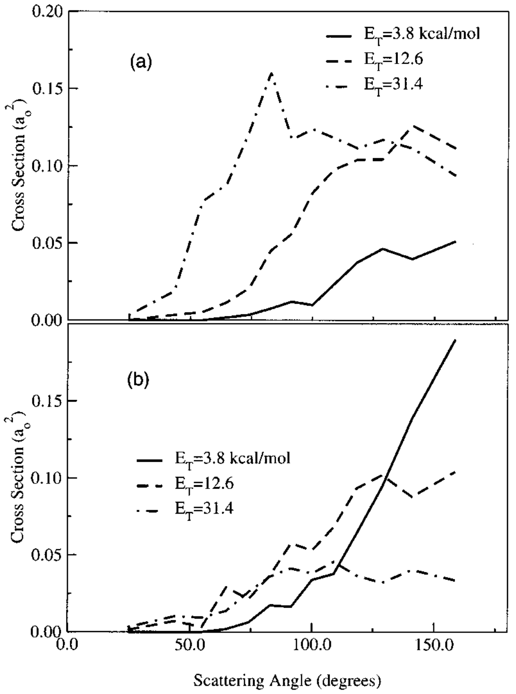

Figure 14. Differential cross section vs scattering angle θ for (R−1), resolved into the (a) v' = 0, and (b) v' = 1 final vibrational states of H_2. Initial QCT conditions were v = 0, J = 0, and E_T = 3.8, 12.6, 31.4 kcal/mol.

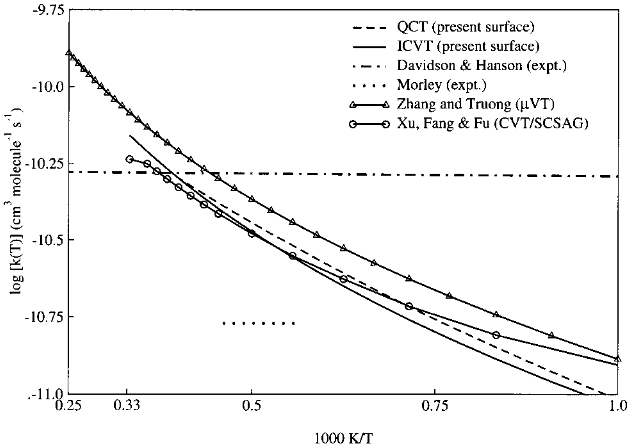

Figure 15. Arrhenius plot of the thermal rate constant for $NH(X^3\Sigma^-) + H \rightarrow N(^4S) + H_2$.

D. Exchange Reaction, $H + NH(X^3\Sigma^-) \rightarrow HN(X^3\Sigma^-) + H$. The QCT results for the exchange reaction have similarities with the forward ($N + H_2$) reaction. Its reaction cross section increases with both translational energy and reagent vibrational excitation but does not vary much for rotational states J = 0−2. For this thermoneutral reaction, there is a significant redistribution of the total energy initially available for the reaction among product degrees of freedom. In Table 4, we can observe a significant loss of the reagent translational energy (ΔE_T = 2.5 kcal/mol), and that this energy is transformed into either vibrational or rotational excitation. We can also see that the product NH vibrational distribution at E_T = 31.4 kcal/mol (v = 0, J = 0) is dominated by v' = 0 (81%), followed by v' = 1 (17%), and v' = 2 (2%), while the average rotational states for these vibrational states are 4, 3, and 1, respectively. Like the forward and reverse abstraction reactions, the exchange reaction also shows a preference for backscattering of the product NH diatoms, in fact, at $E_T = 31.4$ kcal/mol ($v = 0$, $J = 0$), $\langle\theta\rangle_{total} = 145°$, which is significantly more obtuse than the $\langle\theta\rangle$'s found for both the forward and reverse reactions.

IV. Conclusions

In this paper, we demonstrated the sufficiency of the GROW Shepard interpolation program for generating a potential surface for the NHH system that is suitable for performing state-to-state quasiclassical trajectory calculations. The ab initio results were based on high-level MCQDPT2 calculations with FORS-MCSCF(7,6) optimized MO's and the 6-311++G** basis set, and we demonstrated that this level of calculation yields saddle point properties and reaction energetics that are comparable in quality with high-level single reference-based methods that used better basis sets and also with experiment. The GROW-generated PES was based on 156 ab initio points, with gradients and Hessians, and we found that it accurately describes the two linear transition state structures, corresponding to the forward/reverse and exchange reactions, and it yields a surface that is sufficiently smooth so that trajectories are well behaved.

An analytical expression for calculating the Boltzmann *J*-state averaged thermal rate constant was also introduced, which was derived by using a simple 3-parameter analytical function. Using this equation (see eq 3), the thermal QCT rate constant values for (R1) and (R−1) are derived, which can be expressed in the Arrhenius form as $k(\mathrm{T}) = 6.85 \times 10^{-10} \exp(-25.9(\mathrm{kcal/mol})/RT)$ and $k(T) = 1.85 \times 10^{-14}T^{1.07} \exp(-2.2(\mathrm{kcal/mol})/RT)$ cm^3 molecule^{-1} s^{-1}, respectively. These were found to be in good accord with available experimental and theoretical data at temperatures for which measured data are available. This reasonable agreement with available data substantiates the accuracy of the computational methods employed in this study. The calculated k_1 and k_{-1} ICVT rate constants based on the present NHH surface also show excellent agreement with the available experimental and theoretical results. These can be expressed as $k(T) = 5.52 \times 10^{-10} \exp(-32.4(\mathrm{kcal/mol})/RT)$ and $k(T) = 1.56 \times 10^{-16}T^{1.64} \exp(-0.7(\mathrm{kcal/mol})/RT)$ cm^3 molecule^{-1} s^{-1}, respectively. Although the QCT and ICVT Arrhenius parameters are not in good agreement, the rate constants at 2500 K are almost identical for reaction R−1 and they differ by a factor of 4.6 for reaction R1.

The present theoretical analysis also indicates that there is much that can be learned from the dynamics of the title reactions, even in the absence of experimental molecular dynamics data. All three reactions show angular distributions that are backward peaked, consistent with triatomic reactions that have collinear transition state structures. Both the forward abstraction and the exchange reactions show vibrational distributions that are dominated by the product ground vibrational state, whereas the reverse reaction prefers $v' = 1$ for trajectories initiated at low E_T. Product rotational excitation for all the three reactions is found to be a generally increasing function of the reagent E_T.

Acknowledgment. This research was supported by NSF Grant CHE-9873892, by AFOSR MURI Grant F49620-01-1-0335, by the NSF-Hungarian Scientific Research Fund, Hungarian Academy of Sciences (Grant No. 006), and by the Hungarian Scientific Research Grant No. T29726. R.Z.P. acknowledges the Commission on Higher Education, Mindanao Advance Education Program (CHED-MAEP) of the Republic of the Philippines, and the Fulbright−Philippine American Educational Foundation for the six-month research fellowship grant in Northwestern University. It is also a pleasure to acknowledge many helpful conversations and assistance from Eduardo Coronado, Matthew Lakin, Neil Snider, and Fred Arnold. And we thank Michael A. Collins of Australian National University for sharing the GROW program.

Supporting Information Available: Complete set of 156 data points in a format compatible with the GROW program. This information is available free of charge via the Internet at http://pubs.acs.org.

References and Notes

(1) Prasad, K.; Yetter, R. A.; Smooke, M. D. *Combust. Sci. Technol.* **1997**, *124*, 35.

(2) Dove, J. E.; Nip, W. S. *Can. J. Chem.* **1979**, *57*, 689.

(3) Davidson, D. F.; Kohse-Hoingaus, K.; Chang, A. Y.; Hanson, R. K. *Int. J. Chem. Kinet.* **1990**, *22*, 513.

(4) Koshi, M.; Yoshimura, M.; Fukuda, K.; Matsui, H.; Saito, K.; Watanabe, M.; Imamura, A.; Chen, C. *J. Chem. Phys.* **1990**, *93*, 8703.

(5) Davidson, D. F.; Hanson, R. K. *Int. J. Chem. Kinet.* **1990**, *22*, 843.

(6) Morley, C. *Proceedings of the 18th Symposium on Combustion*; The Combustion Institute: Pittsburgh, 1981; p 23.

(7) Baulch, D. L.; Cobos, C. J.; Cox, R. A.; Esser, C.; Frank, P.; Just, T.; Kerr, J. A.; Pilling, M. J.; Troe, J.; Walker, R. W.; Warnatz, J. *J. Phys. Chem. Ref. Data* **1992**, *21*, 411.

(8) Hanson, R. K.; Salimian, S. In *Combustion Chemistry*; Gardiner, W. C., Ed.; Springer: New York, 1984.

(9) Zhang, S.; Truong, T. N. *J. Chem. Phys.* **2000**, *113*, 6149.

(10) Xu, Z. F.; Fang, D. C.; Fu, X. Y. *J. Phys. Chem. A* **1997**, *101*, 4432.

(11) Pederson, L. A.; Schatz, G. C.; Ho, T. S.; Hollebeek, T.; Rabitz, H.; Harding, L. B.; Lendvay, G. *J. Chem. Phys.* **1999**, *110*, 9091.

(12) (a) Wu, G.; Schatz, G. C.; Lendvay, G.; Fang, D.-C.; Harding, L. B. *J. Chem. Phys.* **2000**, *113*, 3150. (b) Schatz, G. C.; Wu, G.; Lendvay, G.; Fang, D.-C.; Harding, L. B. *Faraday Discuss. Chem. Soc.* **1999**, *113*, 151. (c) Braunstein, M.; Duff, J. W. *J. Chem. Phys.* **2000**, *113*, 7406 (d) Gonzalez, M.; Valero, R.; Sayos, R. *J. Chem. Phys.* **2000**, *113*, 10983. (e) Guadagnini, R.; Schatz, G. C. *J. Chem. Phys.* **1995**, *102*, 774.

(13) Casavecchia, P.; Balucani, N.; Volpi, G. G. *Annu. Rev. Phys. Chem.* **1999**, *50*, 347.

(14) Honvault, P.; Launay, J. M. *J. Chem. Phys.* **1999**, *111*, 6665.

(15) Balucani, N.; Alagia, M.; Cartechini, L.; Casavecchia, P.; Volpi, G. G.; Pederson, L.; Schatz, G. C. *J. Phys. Chem.* A **2001**, *105*, 2414.

(16) (a) Jordan, M. J. T.; Thompson, K. C.; Collins, M. A. *J. Chem. Phys.* **1995**, *102*, 5647. (b) Thompson, K. C.; Jordan, M. J. T.; Collins, M. A. *J. Chem. Phys.* **1998**, *108*, 8302. (c) Bettens, R. P. A.; Collins, M. A. *J. Chem. Phys.* **1999**, *111*, 816. (d) Thompson, K. C.; Collins, M. A. *J. Chem. Soc., Faraday Trans.* **1997**, *93*, 871.

(17) Schmidt, M. W.; Baldridge, K. K.; Boatz, J. A.; Elbert, S. T.; Gordon, M. S.; Jensen, J. H.; Koseki, S.; Matsunaga, N.; Nguyen, K. A.; Su, S. J.; Windus, T. L.; Dupuis, M.; Montgomery, J. A. *J. Comput. Chem.* **1993**, *14*, 1347−1363. GAMESS v. 25 March 2000 from Iowa State University.

(18) Frisch, M. J.; Trucks, G. W.; Schlegel, H. B.; Scuseria, G. E.; Robb, M. A.; Cheeseman, J. R.; Zakrzewski, V. G.; Montgomery, J. A., Jr.; Stratmann, R. E.; Burant, J. C.; Dapprich, S.; Millam, J. M.; Daniels, A. D.; Kudin, K. N.; Strain, M. C.; Farkas, O.; Tomasi, J.; Barone, V.; Cossi, M.; Cammi, R.; Mennucci, B.; Pomelli, C.; Adamo, C.; Clifford, S.; Ochterski, J.; Petersson, G. A.; Ayala, P. Y.; Cui, Q.; Morokuma, K.; Malick, D. K.; Rabuck, A. D.; Raghavachari, K.; Foresman, J. B.; Cioslowski, J.; Ortiz, J. V.; Baboul, A. G.; Stefanov, B. B.; Liu, G.; Liashenko, A.; Piskorz, P.; Komaromi, I.; Gomperts, R.; Martin, R. L.; Fox, D. J.; Keith, T.; Al-Laham, M. A.; Peng, C. Y.; Nanayakkara, A.; Gonzalez, C.; Challacombe, M.; Gill, P. M. W.; Johnson, B.; Chen, W.; Wong, M. W.; Andres, J. L.; Gonzalez, C.; Head-Gordon, M.; Replogle, E. S.; Pople, J. A. *Gaussian 98*, Revision A.7; Gaussian, Inc.: Pittsburgh, PA, 1998.

(19) Steckler, R.; Chuang, Y.-Y.; Coitiño, E. L.; Hu, W.-P.; Liu, Y.-P.; Lynch, G. C.; Nguyen, K. A.; Jackels, C. F.; Gu, M. Z.; Rossi, I.; Fast, P.; Clayton, S.; Melissas, V. S.; Garrett, B. C.; Isaacson, A. D.; Truhlar, D. G. POLYRATE-7.0, University of Minnesota, Minneapolis, 1996.

(20) Truhlar, D. G.; Isaacson, A. D.; Garrett, B. C. *Theory of Chemical Reaction Dynamics*; Baer, M., Ed.; CRC Press: Boca Raton, FL, 1985; Vol. IV, p 65.

(21) (a) Troya, D.; Lakin, M. J.; González, M.; Schatz, G. C. *J. Chem. Phys.* **2001**, *115*, 1828. (b) Goldfield, E. M.; Gray, K. S. To be published.

(22) (a) Aoiz, F. J.; Bañares, L.; Herrero, V. J.; Rábanos, V. S.; Stark, K.; Werner, H. J. *J. Chem. Phys.* **1995**, *102*, 9248. (b) Balucani, N.; Cartechini, L.; Casavecchia, P.; Volpi, G. G.; Aoiz, F. J.; Bañares, L.; Menéndez, M.; Bian, W.; Werner, H.-J. *Chem. Phys. Lett.* **2000**, *328*, 500. (c) Schatz, G. C.; Pederson, L. A.; Kuntz, P. J. *Faraday Discuss.* **1997**, *108*, 357. (d) Ron, S.; Baer, M.; Polak, E. *J. Chem. Phys.* **1983**, *78*, 4414.

(23) Aker, P. M.; Germann, G. J.; Tabor, K. D.; Valentini, J. J. *J. Chem. Phys.* **1989**, *90*, 4809.

(24) Aoiz, F. J.; Herrero, V. J.; Rábanos, V. S. *J. Chem. Phys.* **1991**, *94*, 7991.

(25) Polanyi, J. C.; Wong, W. H. *J. Chem. Phys.* **1969**, *51*, 1439.

(26) Mayer, S. W.; Schieler, L. *J. Phys. Chem.* **1968**, *72*, 236.